



Investigation of the metastable spinodally decomposed magnetic CrFe-rich phase in Al doped CrFeCoNi alloy

Esmat Dastanpour^{a,*}, Shuo Huang^{b,c}, Zhihua Dong^{d,e}, Stephan Schönecker^a, Valter Ström^a, Olle Eriksson^{c,f}, Lajos Károly Varga^g, Levente Vitos^{a,c,g}

^a Department of Materials Science and Engineering, KTH Royal Institute of Technology, Stockholm SE-100 44, Sweden

^b Faculty of Materials Science and Chemistry, China University of Geosciences, Wuhan 430074, China

^c Department of Physics and Astronomy, Division of Materials Theory, Uppsala University, Uppsala SE-751 20, Sweden

^d National Engineering Research Center for Magnesium Alloys, College of Materials Science and Engineering, Chongqing University, Chongqing 400044, China

^e Chongqing Institute for Advanced Light Metals, Chongqing 400030, China

^f School of Science and Technology, Örebro University, Örebro SE-701 82, Sweden

^g Institute for Solid State Physics and Optics, Wigner Research Centre for Physics, Budapest H-1525, Hungary

ARTICLE INFO

Article history:

Received 14 September 2022

Received in revised form 22 December 2022

Accepted 7 January 2023

Available online 9 January 2023

Keywords:

High entropy alloy

AlCrFeCoNi

Spinodal decomposition

Structural transformation

Magnetization

ABSTRACT

We have conducted an in-depth study of the magnetic phase due to a spinodal decomposition of the BCC phase of a CrFe-rich composition. This magnetic phase is present after casting (arc melting) or water quenching after annealing at 1250 °C for 24 h but is entirely absent after annealing in the interval 900–1100 °C for 24 h. Its formation is favored in the temperature interval ca 450–550 °C and loses magnetization above 640 °C. This ferromagnetic-paramagnetic transition is due to a structural transformation from ferromagnetic BCC into paramagnetic σ and FCC phases. The conclusion from measurements at different heating rates is that both the transformation leading to the increase of the magnetization due to the spinodal decomposition of the parent phase and the vanishing magnetization at 640 °C are diffusion controlled.

© 2023 The Authors. Published by Elsevier B.V. This is an open access article under the CC BY license (<http://creativecommons.org/licenses/by/4.0/>).

1. Introduction

High entropy alloys (HEAs) are multi-component systems containing five or more elements with concentrations from 5 to 35 at% for each principal element [1–4]. HEAs may be single phase, form dual or multiple phase equilibria, and exhibit intermetallic compounds with complex structures [5–7]. Solid solution phases in HEAs typically form simple structures, i.e., face-centered-cubic (FCC), body-centered cubic (BCC), or hexagonal close-packed (HCP) structures. Many of these alloys exhibit interesting properties, such as high mechanical strength, excellent thermal stability, outstanding resistance to corrosion, wear, and fatigue, and special electrical and magnetic properties [8,9]. Owing to a combination of unique functional and structural properties, these new materials are the subject of increasing attention in material science since firstly proposed by Yeh et al. [10,11].

The Al_xCrFeCoNi HEA is one of the most investigated multi-component alloy systems [12]. The crystal structure undergoes an

FCC to BCC structural transformation with increasing Al amount, and a disordered BCC phase combined with an ordered B2 phase appear at high Al concentrations [13,14]. This structural transition fundamentally dictates all electronic properties including magnetism, inasmuch as at room temperature the FCC phase is essentially paramagnetic, whereas the BCC phase is ferromagnetic with a substantial saturation magnetization [15,16].

It is known that the Al content itself does not affect the magnetic properties much, but instead it is the structure (FCC vs. BCC) and the exact composition of the CrFeCoNi content that is decisive. Moreover, the Al_xCrFeCoNi system often has a tendency to form a Cr-rich σ phase, which embrittles the alloy at high temperatures [17].

Several studies focused on the structural and magnetic properties of the AlCrFeCoNi HEA [18–21]. For example, the study of Manzonei et al. [21] showed that the microstructure of this alloy contains CrFe-rich precipitates embedded in an Al-Ni rich homogeneous matrix. Atom probe tomography investigation by the same authors revealed nano-scale fluctuations of Fe- and Cr-rich domains in Cr-Fe rich precipitates, which was attributed to spinodal decomposition. Shivam et al. [19] demonstrated that AlCrFeCoNi HEA prepared by mechanical alloying and sintering has promising soft

* Corresponding author.

E-mail address: Esmatdh@kth.se (E. Dastanpour).

magnetic properties with saturation magnetization of 70.05 Am²/kg along with effective Curie temperature of 617 °C.

In this work, we initially studied the structural and magnetic properties of the AlCoCrFeNi system after various heat treatments. However, the results were not exhaustive, and in particular, the nature of the disappearance of magnetization at 640 °C was not established. Therefore, we prepared a 'model' composition (Al₆Cr₃₇Fe₂₄Co₂₁Ni₁₂ at%) after an elemental analysis of the magnetic phase in the original material. This enabled us to clarify both the appearance of a magnetic phase in the temperature interval 450–550 °C as due to a diffusion-controlled spinodal decomposition as well as its dissolution and the concomitant disappearance of the magnetization at 640 °C.

2. Experimental

The HEA ingot with a nominal composition of AlCrFeCoNi was prepared using arc melting of high purity metals (Fe, Co, Ni, Cr, and Al). Approximately 2–3 g of raw materials was arc melted in a water-cooled copper mold under ultrahigh-purity argon. Each ingot was remelted 4 times to improve chemical homogeneity.

Annealing of the ingots was carried out at a temperature of 900 °C, 1000 °C, 1100 °C, and 1250 °C for 24 h in a tube furnace under argon flow. The heated ingots were quenched in water.

The structures of the as-cast and annealed ingots were identified by X-ray diffraction (XRD) analysis (model SIEMENS D5000) by using Cu K α radiation with a graphite monochromator in 30 deg $\leq 2\theta \leq 100$ deg. The volume fractions of B2 and BCC phases was determined by Rietveld refinement using the MAUD (Material Analysis Using Diffraction) software and the required crystallographic information files for the BCC and B2 structures were taken from the Crystallography Open Database [22,23].

The as-cast and annealed samples were sectioned, sanded with emery paper and finally polished with 0.05 μ m colloidal Silica. The polished faces were observed under a scanning electron microscope (SEM, Hitachi). The chemical compositions were determined by an energy dispersive spectrometer (EDS, Oxford Instruments, X-Max, England) operating at 15 kV.

Electron back scattered diffraction (EBSD) measurements were carried out on polished specimens using a FIB Nova600 operated at 20 kV. The AZtecHLK software (Oxford Instruments, UK) was used for the analysis.

Atomic-scale characterization of the as-cast sample was performed using atom probe tomography (APT). The nano-tips (40 nm diameter) for APT were prepared by focused ion beam (FIB) milling using Ga ions in a FIB Nova 600 operated at 30 kV, with final cleaning at 5 kV. The APT tips were field evaporated at a specimen temperature of 60 K by laser pulsing with a 3 nJ pulse energy at 200 kHz repetition rate, using an ELKOS-UV instrument. Data reconstruction and analysis were carried out using the APSuite software provided by Cameca.

Magnetic properties were investigated with a vibrating sample magnetometer (VSM, EG&G model 155) under an applied field of 600 kA/m. The magnetization dependence of temperature, $M(T)$, was determined with magneto-thermo-gravimetry (MTG, TGS2 Perkin-Elmer) in the temperature range of 50–800 °C and different heating rates in argon flow. The results are the quotient between the recorded force due to a permanent magnet located at a fixed distance below the sample and the samples' gravitational force [24].

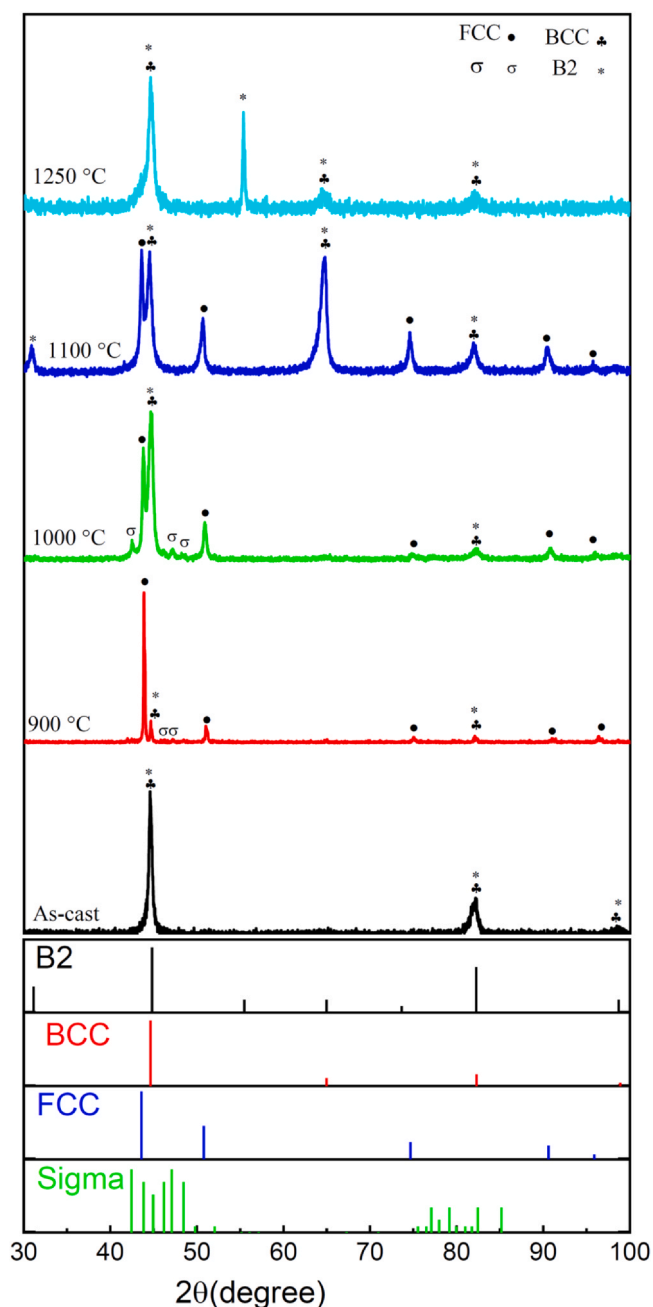


Fig. 1. The XRD patterns of as-cast and annealed AlCrFeCoNi alloy (annealed at 900 °C, 1000 °C, 1100 °C, and 1250 °C for 24 h and quenched in water). The standard peaks of FCC, BCC, B2 and σ are shown in the lower panel.

3. Results and discussion

3.1. Structural and magneto-thermo-gravimetric results of annealing

Fig. 1 shows the XRD patterns of the as-cast and annealed samples. From the XRD investigation and SEM studies, we conclude the following sequence of phase content:

- As-cast: BCC/B2.
- 900 °C: FCC + σ + minor BCC/B2.
- 1000 °C: FCC + σ + BCC/B2.
- 1100 °C: FCC + BCC/B2.
- 1250 °C: BCC/B2.

These results are in line with previous studies on the phase transitions in AlCrFeCoNi HEA [6,25]. It should be noted that the

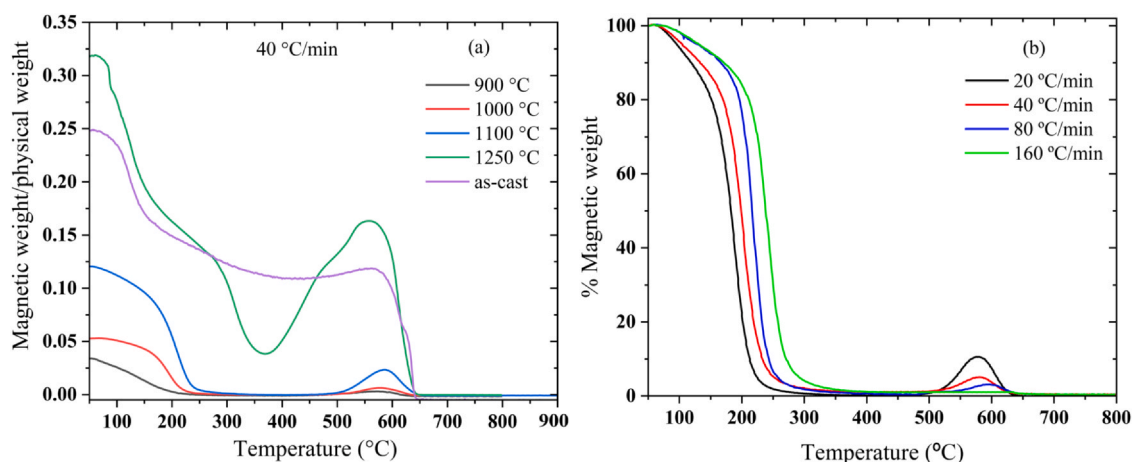


Fig. 2. (a) Magnetization as a function of temperature $[M(T)]$ recorded as ratio of magnetic weight to sample weight for the as-cast and annealed AlCrFeCoNi alloy (900–1250 °C) at a heating rate of 40 °C/min. (b) The magnetic weight in percent of the weight at the starting temperature, i.e., 50 °C, as a function of temperature measured by the MTG at different heating rates of 20, 40, 80, and 160 °C/min for different specimens of the annealed sample at 1000 °C. Magnetic field is ca 3 kA/m.

peaks of the B2 phase often are difficult to observe in the XRD patterns due to a very similar (but not identical) lattice constant as the BCC phase. We confirmed the presence of the B2 phase in the as-cast sample (approximate volume fraction is 15%) by a Rietveld refinement (result not shown). The presence of this phase has also been confirmed in other studies in similar systems by high resolution techniques, e.g., transmission electron microscopy (TEM) [26].

Three distinct features from the magneto-thermo-gravimetric (MTG) measurements shown in Fig. 2 for the annealed samples (900–1000–1100 °C) are i) a complete disappearance of magnetization at ca 230 °C ii) an evolving magnetization in the temperature interval of ca 450–550 °C, which we attribute to the appearance of a magnetic phase due to a partial structural transformation from a paramagnetic phase into a magnetically ordered phase and iii) a complete disappearance of magnetization around 640 °C.

To clearly show that the evolution of the magnetic phase disappearing at 640 °C is time dependent, i.e., diffusion controlled, we performed a sequence of MTG measurements with different heating rates for the material annealed at 1000 °C. From Fig. 2b it can be concluded that the development of the magnetic phase is time dependent. At lower heating rates, the ratio of magnetic weight to physical weight is larger. We should also notice that the disappearance of the magnetization around 640 °C is shifted towards higher temperatures with increasing heating rate.

The MTG measurements (Fig. 2a) on the as-cast material and the 1250 °C annealed material are quite different compared to the 900–1000–1100 °C annealed materials. The magnetization is ca 5 times stronger at room temperature (RT) and does not disappear at ca 230 °C. Instead, we see a significant reduction approx. at 150 °C. However, a slight – or a more pronounced for the 1250 °C material – increase in magnetization in the 450–550 °C interval is observed. However, ferromagnetism vanishes at 640 °C, similarly to the three annealed alloys.

Hence, the disappearance of magnetization at 640 °C is universal in all the investigated samples – annealed or as-cast – which suggests that the phases in question and the mechanisms are identical or very similar. This will be studied in more detail further on.

3.2. Determination of the chemical compositions of the constituent phases

Fig. 3 shows the SEM images obtained for the as-cast and annealed samples. The chemical compositions of different zones are presented in Table 1. Within the spatial resolution limit of SEM, the as-cast alloy shows a completely uniform composition on the

micrometer scale ($\text{Al}_{19.6}\text{Cr}_{20.1}\text{Fe}_{20.4}\text{Co}_{20.3}\text{Ni}_{19.8}$ at%). For the alloy annealed at 900 °C, the SEM images show two distinct zones (image contrasts). However, their chemical compositions could not be accurately determined due to the small spatial scale variation in the morphology. Taken together, our XRD and SEM results suggest that the dominant phase (B zone) is the FCC phase, whereas the dark (D) zone with a weave-like morphology is attributed to the BCC/B2 phase.

With increasing the annealing temperature to 1000 and 1100 °C, besides the D and B zones, the microstructure contains a gray zone (G). By considering the chemical compositions of the various observed zones shown in Table 1 in combination with the XRD results, we suggest that the bright zone is the major, FCC phase (as in the sample annealed at 900 °C), the dark (AlNi-rich) zone is the B2 phase, and the gray (CrFe-rich) zone is the BCC phase. It should be noted that the XRD patterns for annealed alloys at 1000 and 1100 °C shows peaks of the σ phase. However, the identification of the σ phase on the SEM images was not possible due to the similar chemical compositions of the σ and BCC phases. The study of the chemical compositions of the BCC phase and the σ phase by Meshi et al. [17] with the EDS analysis in TEM showed the chemical composition of $\text{Al}_2\text{Cr}_{43}\text{Fe}_{29}\text{Co}_{20}\text{Ni}_6$ and $\text{Al}_1\text{Cr}_{48}\text{Fe}_{26}\text{Co}_{20}\text{Ni}_5$ (at%) for the BCC and σ phases, respectively, consistent with our results.

In the alloy annealed at 1250 °C, besides of a weave-like morphology, a morphology of spherical particles embedded in the matrix appears. The latter finding is similar to what Ma et al. [26] found in an investigation of $\text{Al}_x\text{CrFeCoNi}$ HEAs with high amounts of Al. They reported two morphologies in the BCC/B2 region with high Al content, namely a weave-like pattern related to the BCC/B2 phase and the ordered B2 matrix, with some disordered BCC precipitates with a spherical morphology.

Atomic-scale distributions of elements in the as-cast sample is shown in Fig. 4. The three-dimensional distributions of elements presented in Fig. 4a and the one-dimensional concentration profiles in Fig. 4b reveal the formation of a AlNi-rich phase (left and right hand regions) and CrFe-rich phase (center region). Co is homogeneously distributed (about 20 at%) in both phases. The anti-correlated fluctuations of Cr and Fe elements in the CrFe-rich phase confirms the spinodal decomposition in this phase. The iso-concentration surface (corresponding to 40.3 at% Cr) in the CrFe-rich phase is shown in Fig. 4c. The concentration profile in the proximity of the interface between Cr-rich segregation and the Cr deficient matrix clearly show a decomposition of the CrFe-rich phase into Cr-rich phase and FeCo-rich sub-phases.

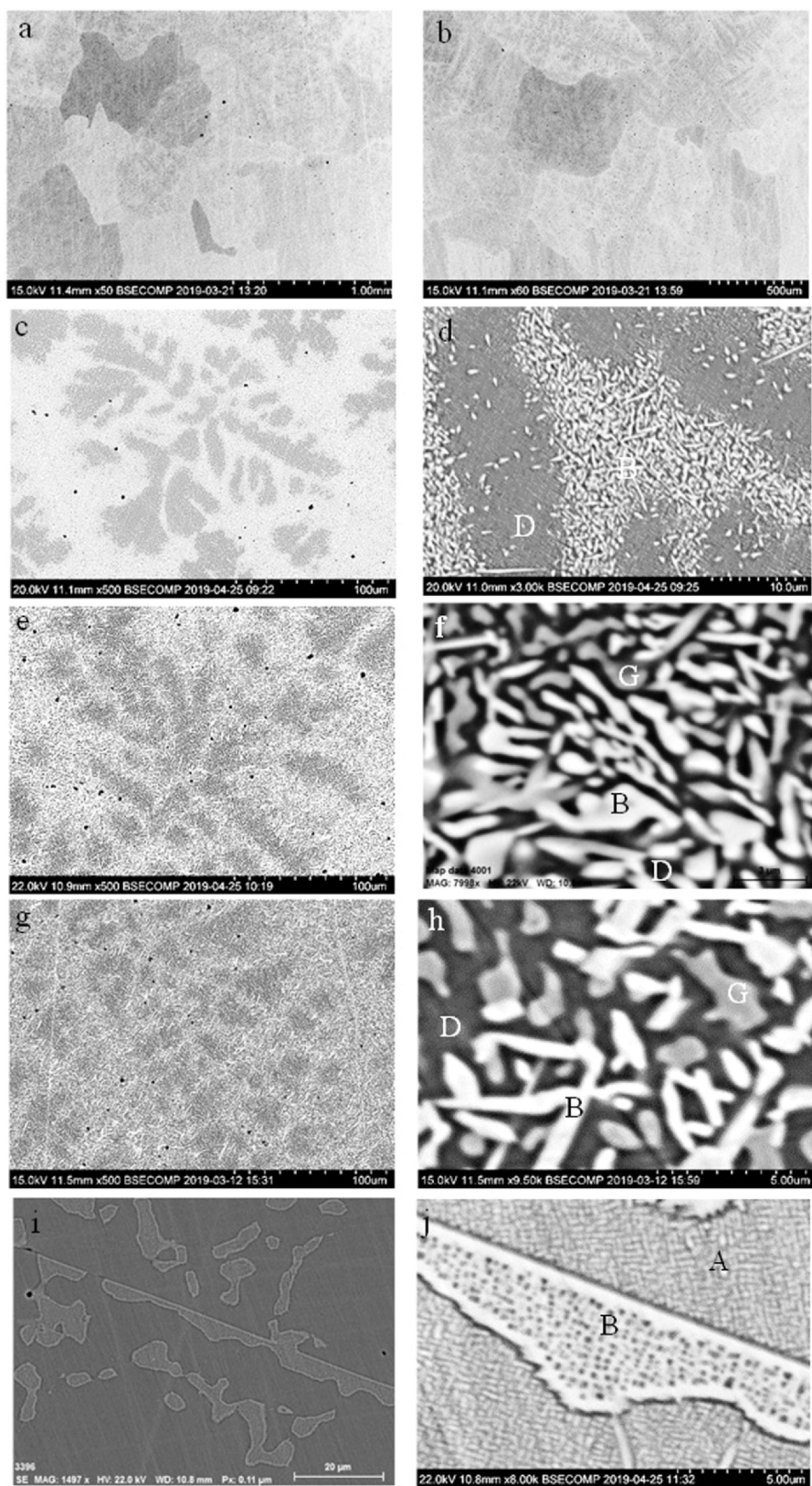


Fig. 3. SEM images of AlCrFeCoNi alloy in the as-cast state (a)–(b) and annealed state where annealing temperature was (c)–(d) 900 °C, (e)–(f) 1000 °C, (g)–(h) 1100 °C, (i)–(j) 1250 °C. Left-hand and right-hand panels were taken with low and high resolution, respectively.

3.3. Explanation of the structural and magnetic results

We provide the following explanation for the observed results. The magnetic contribution evolving in the 450–550 °C interval and

its heating rate dependence is due to a spinodal decomposition of a CrFe-rich BCC phase (which incidentally is the result of the phase decomposition of the main composition) into a Cr-rich (para-magnetic) component and a magnetic FeCo-rich component, as

Table 1

Chemical compositions of different zones of the annealed samples corresponding to the SEM images presented in Fig. 3. Highlighted in bold is the composition of the model alloy discussed in Section 3.4.

Temperature (°C)	Area	Structure	Designation	Chemical composition (at%)				
				Al	Cr	Fe	Co	Ni
900	Dark zone (D)	BCC*/B2	CrFe rich/AlNi-rich	22.2	16.1	18.4	21.1	22.2
	Bright zone (B)	FCC		15.9	17.7	22.7	23.9	19.8
1000	Dark zone (D)	B2	AlNi-rich	26.9	13.9	15.6	19.6	24.0
	Bright zone (B)	FCC		11.3	29.1	24.1	20.7	14.8
1100	Gray zone (G)	BCC*	CrFe rich	5.9	37.1	24.1	21.1	11.8
	Dark zone (D)	B2	AlNi-rich	26.1	13.7	15.0	19.9	25.3
	Bright zone (B)	FCC		6.3	25.8	29.3	25.3	13.3
1250	Gray zone (G)	BCC	CrFe rich	4.5	41.1	27.7	19.7	7.0
	A	BCC/B2	CrFe rich/AlNi-rich	17.6	21.9	20.5	19.2	20.8
	B	BCC/B2	CrFe rich/AlNi-rich	12.6	25.7	24.1	22.0	15.6

* The identification of the σ phase and the BCC phase is not possible in this measurement as the chemical compositions of these two phases are very similar.

observed by atom probe tomography (APT) [18,27–29]. We suggest that the magnetization drop at ca 150 °C for the as-cast and the 1250 °C annealed samples is due to an undecomposed CrFe-rich BCC phase. This suggestion is consistent by our previous independent ab initio calculation [30].

The samples annealed at 900–1000–1100 °C are relatively less magnetic at RT, and have a T_C of approximately 230 °C, although magnetization and to some extent also the T_C increase with increased annealing temperature. We suggest that this magnetization is due to increased amounts of the BCC/B2 phases with increased annealing temperature, supported by the XRD results. At this point we refrain from suggesting the responsible magnetic phase(-es). However, in these alloys the dominant fraction is an FCC phase with a significant σ -content (900–1000 °C annealed samples), which are both paramagnetic at room temperature.

The RT hysteresis loops in Fig. 5 are consistent with this reasoning: both the as-cast and 1250 °C annealed samples have a saturation magnetization of around 55 Am²/kg, whereas the 900–1000–1100 °C annealed samples have much lower magnetization, i.e., ca 10–20 Am²/kg. Moreover, the former (Fig. 5a) also display a distinct coercivity, ca H_c = 10 kA/m, of which we do not have any viable explanation at this point.

An important aspect in this scenario is the origin of the disappearance of magnetization at 640 °C. Superficially it might appear as a proper T_C – Curie point – due to its invariant dependence on heating rate and exact phase composition. As explained before, the BCC phase decomposed into paramagnetic Cr-rich and ferromagnetic FeCo-rich phases. The measured T_C for the FeCo-rich phase with the chemical composition taken from [18], confirms that the disappearance of magnetization at 640 °C should be a structural transition instead of a magnetic transition due to the high T_C (ca 900 °C) of the FeCo-rich phase. Therefore, we conducted a detailed study to identify the mechanism.

3.4. Characterization and verification of the magnetic spinodal decomposed phase

To understand the magnetic transition at 640 °C, a model alloy with the nominal composition of the gray zone in the sample annealed at 1000 °C (Al₆Cr₃₇Fe₂₄Co₂₁Ni₁₂ at%) and suggested BCC structure was prepared by arc-melting (Fig. 6a).

This as-cast specimen shows an increase of magnetization (Fig. 6b) in the 450–550 °C interval, attributed to a more intense spinodal decomposition at higher temperatures, and exhibits a rapid drop of magnetization to zero at 640 °C. The Fig. 6c shows that the

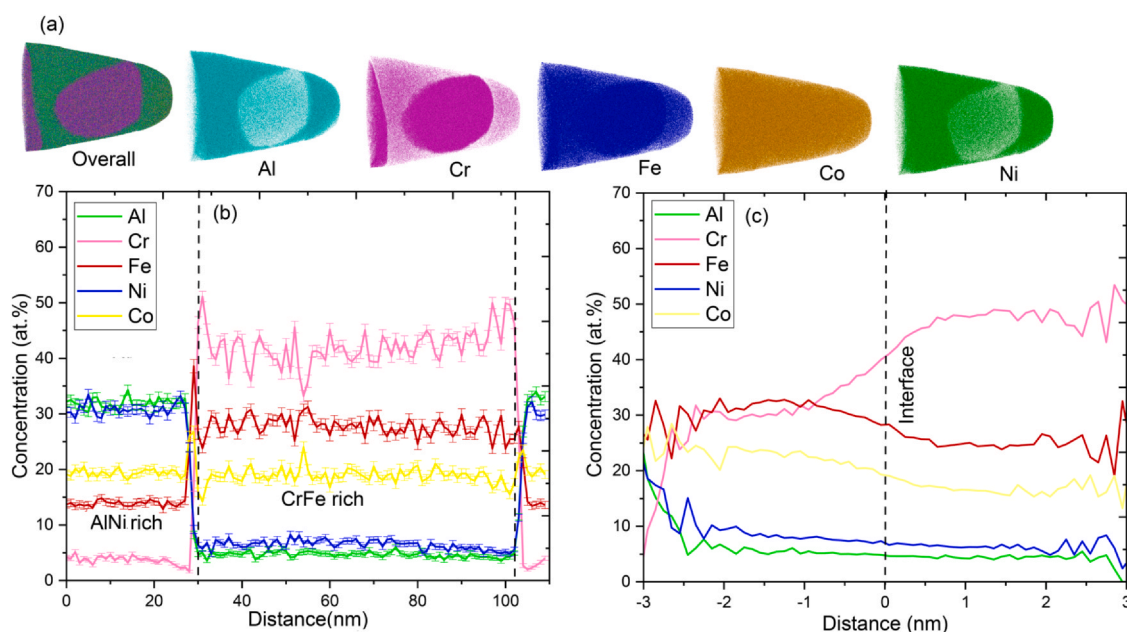


Fig. 4. APT analysis of the as-cast AlCoCrFeNi alloy (a) three-dimensional distributions of Al, Co, Cr, Fe and Ni atoms, (b) one-dimensional concentration profiles of elements (with 0.3 nm bin width) taken along a cylinder (of 10 nm diameter) and (c) the proximity histogram (with 0.1 nm bin width) for iso-concentration surfaces highlighting the 40.3 at% Cr region in the CrFe-rich phase.

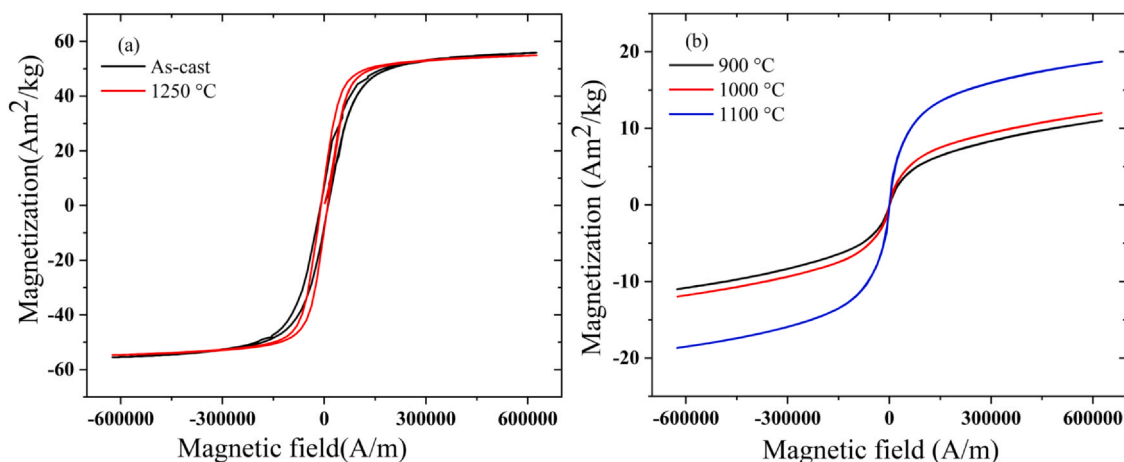


Fig. 5. The hysteresis loops at the maximum field, ca 600 kA/m for a) the as-cast and 1250 °C annealed samples, b) alloy annealed at 900, 1000, and 1100 °C.

saturation magnetization of the as-cast alloy is about 60 Am²/kg. After performing the MTG measurement with heating rate of 40 °C/min up to 650 °C and cooling, the sample is paramagnetic at RT. This can be explained by the transition of the main BCC structure in the

as-cast alloy to the σ and FCC phases during the MTG measurement. XRD patterns recorded before and after the MTG measurement in Fig. 6a corroborate this picture.

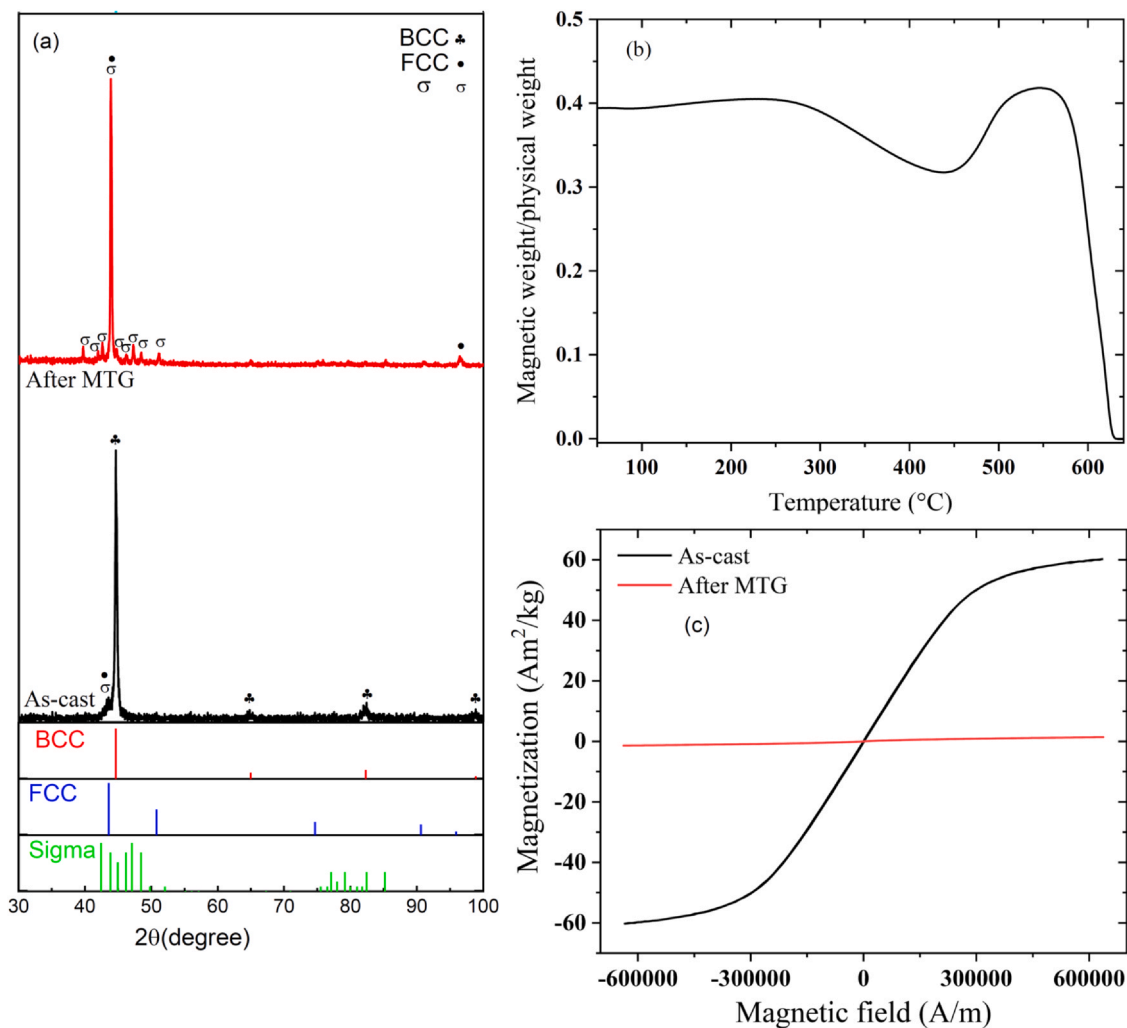


Fig. 6. (a) The XRD patterns for Al₆Cr₃₇Fe₂₄Co₂₁Ni₁₂ alloy in the as-cast state and after the MTG measurement. The standard peaks of BCC, FCC, and σ are shown in the lower panel. (b) magnetization as a function of temperature [$M(T)$] recorded as ratio of magnetic weight to sample weight for Al₆Cr₃₇Fe₂₄Co₂₁Ni₁₂ alloy (as-cast) at a heating rate of 40 °C/min up to 650 °C. (c) the hysteresis loops before and after the MTG measurement. This experiment shows that only approximately one minute at 640–650 °C is sufficient to enable a complete structural transformation.

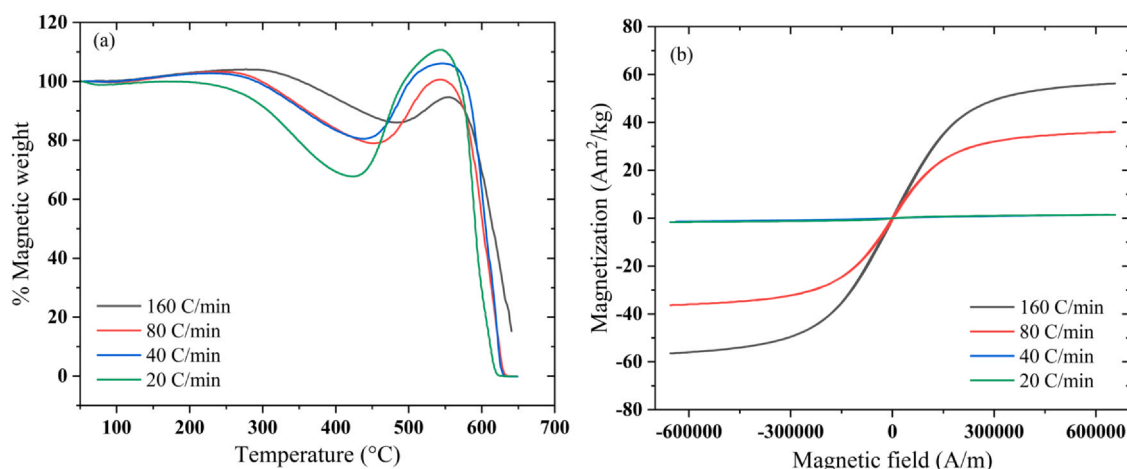


Fig. 7. (a) Magnetic weight in percent of the weight at the starting temperature, i.e., 50 °C, as a function of temperature measured by the MTG of different specimens of the as-cast $\text{Al}_6\text{Cr}_{37}\text{Fe}_{24}\text{Co}_{21}\text{Ni}_{12}$ alloy at different heating rates of 20, 40, 80, and 160 °C/min. (b) RT hysteresis loops for the model alloy after undergoing a single MTG run at various heating rates of 20, 40, 80, and 160 °C/min.

To understand the effect of heating rate on the structural transition, the magnetization as a function of temperature was studied for different specimens of the as-cast model alloy at different heating rates of 20, 40, 80, and 160 °C/min (Fig. 7a). It is observed that shorter heating time (higher heating rates) leads to a shallower hump assigned to the spinodal decomposition in the interval 450–640 °C.

The hysteresis loops of these samples presented in Fig. 7b confirm the pronounced effect of heating rate in MTG measurements on the thereafter recorded RT magnetization curves. Plotted on the same scale, at 160 °C/min the magnetization at RT is essentially unaffected vs. the as-cast material, at 80 °C/min the saturation magnetization has dropped to ca half that value, and at the lower rates (20 and 40 °C/min) ferromagnetism is virtually absent. We attribute this effect to an incomplete structural transition of the BCC phase to the σ and FCC phases at the higher heating rates. An EBSD analysis (Fig. 8) for the model alloy after undergoing a single MTG run at the heating rates of 40 and 160 °C/min reveals a complete transition of the BCC phase to the σ and FCC phases for the case of 40 °C/min, whereas the main phase for the sample annealed at 160 °C/min is still the BCC phase.

This result is proof that the disappearance of the magnetic phase is due to the dissolution of the spinodally decomposed magnetic BCC

phase into paramagnetic σ and FCC phases. The transformation is diffusion controlled.

4. Conclusion

We have investigated the AlCrFeCoNi HEA. The phase content and magnetic properties are highly dependent on preparation and heat treatment procedures. From structural (XRD, SEM, APT) investigations, we have concluded that the main phases in this alloy are i) an undecomposed CrFe-rich BCC phase, ii) a AlNi-rich B2 phase (≈ 20 at% Co in both the B2 and BCC phases), iii) FCC and σ phases, and iv) spinodal decomposition of the CrFe-rich BCC phase into a magnetic FeCo-rich and a paramagnetic Cr-rich phases. Contributing to the complexity is i) the BCC and the B2 phases in the system have very similar lattice constants and ii) the magnetic phase with the highest T_C is due to a spinodal decomposition at a very fine length scale. This spinodal decomposition occurs in the temperature range 450– ca. 550 °C and is dissolved above 640 °C in a structural phase transformation into paramagnetic σ and FCC phases. We suggest that the as-cast (arc-melted) and 1250 °C annealed materials consist of varying proportions of BCC, B2, and spinodally decomposed phases, of which some or all may be magnetic at room temperature. The 900–1000–1100 °C annealed materials lack the spinodally

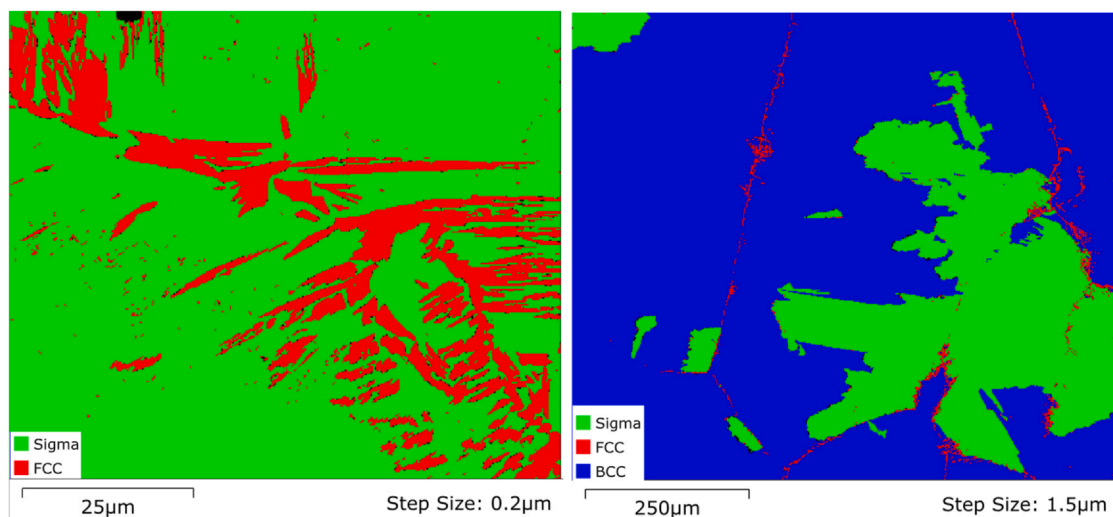


Fig. 8. The EBSD images of the model alloy taken after the MTG measurement with the heating rates of 40 and 160 °C/min.

decomposed phase and as such is paramagnetic above 230 °C. This phase is characterized by distinct FCC and σ content. The disappearance of the spinodally decomposed magnetic phase is universal to all investigated samples and is due to a diffusion-controlled structural transformation at a rather narrow temperature range of a couple of degrees around 640 °C.

CRedit authorship contribution statement

Esma Dastanpour: Conceptualization, Methodology, Formal analysis, Investigation, Data curation, Writing – original draft, Visualization. **Shuo Huang:** Software, Validation, Formal analysis, Investigation, Writing – review & editing, Visualization. **Zhihua Dong:** Software, Validation, Formal analysis, Investigation, Writing – review & editing. **Stephan Schönecker:** Software, Validation, Writing – review & editing, Funding acquisition. **Valter Ström:** Methodology, Validation, Investigation, Resources, Writing – review & editing, Supervision. **Olle Eriksson:** Investigation, Writing – review & editing, Funding acquisition. **Lajos Károly Varga:** Methodology, Investigation, Resources, Writing – review & editing. **Levente Vitos:** Conceptualization, Validation, Investigation, Writing – review & editing, Supervision, Funding acquisition.

Data Availability

No data was used for the research described in the article.

Declaration of Competing Interest

The authors declare that they have no known competing financial interests or personal relationships that could have appeared to influence the work reported in this paper.

Acknowledgement

This work was supported by the Swedish Foundation for Strategic Research, the Swedish Research Council (Grant Agreement No. 2017-06474 and 2019-04971), the Sweden's Innovation Agency (VINNOVA Grant No. 2019-05111), the Carl Tryggers Foundation (Grant Agreement No. 19:325 and 20:474), and the Hungarian Scientific Research Fund (OTKA No. 128229). The authors would like to acknowledge Alexander Dahlström in KTH Stockholm who assisted in APT measurement and characterization.

References

- [1] S. Uporov, V. Bykov, S. Pryanichnikov, A. Shubin, N. Uporova, Effect of synthesis route on structure and properties of AlCoCrFeNi high-entropy alloy, *Intermetallics* 83 (2017) 1–8, <https://doi.org/10.1016/j.intermet.2016.12.003>
- [2] E.P. George, D. Raabe, R.O. Ritchie, High-entropy alloys, *Nat. Rev. Mater.* 4 (2019) 515–534, <https://doi.org/10.1038/s41578-019-0121-4>
- [3] M.C. Gao, D.B. Miracle, D. Maurice, X. Yan, Y. Zhang, J.A. Hawk, High-entropy functional materials, *J. Mater. Res.* 33 (2018) 3138–3155, <https://doi.org/10.1557/jmr.2018.323>
- [4] P.F. Yu, H. Cheng, L.J. Zhang, H. Zhang, M.Z. Ma, G. Li, P.K. Liaw, R.P. Liu, Nanotwin's formation and growth in an AlCoCuFeNi high-entropy alloy, *Scr. Mater.* 114 (2016) 31–34, <https://doi.org/10.1016/j.scriptamat.2015.11.032>
- [5] S. Huang, Z. Dong, W. Mu, V. Ström, G. Chai, L. Vitos, Thermo-elastic properties of bcc Mn-rich high-entropy alloy, *Appl. Phys. Lett.* 117 (2020) 1–6, <https://doi.org/10.1063/5.0017989>
- [6] W.R. Wang, W.L. Wang, J.W. Yeh, Phases, microstructure and mechanical properties of AlxCoCrFeNi high-entropy alloys at elevated temperatures, *J. Alloy. Compd.* 589 (2014) 143–152, <https://doi.org/10.1016/j.jallcom.2013.11.084>
- [7] K. Jasiewicz, J. Cieslak, S. Kaprzyk, J. Tobola, Relative crystal stability of AlxFeNiCrCo high entropy alloys from XRD analysis and formation energy calculation, *J. Alloy. Compd.* 648 (2015) 307–312, <https://doi.org/10.1016/j.jallcom.2015.06.260>
- [8] D.B. Miracle, O.N. Senkov, A critical review of high entropy alloys and related concepts, *Acta Mater.* 122 (2017) 448–511, <https://doi.org/10.1016/j.actamat.2016.08.081>
- [9] Y.F. Kao, T.J. Chen, S.K. Chen, J.W. Yeh, Microstructure and mechanical property of as-cast, -homogenized, and -deformed AlxCoCrFeNi (0 ≤ x ≤ 2) high-entropy alloys, *J. Alloy. Compd.* 488 (2009) 57–64, <https://doi.org/10.1016/j.jallcom.2009.08.090>
- [10] J.W. Yeh, S.K. Chen, S.J. Lin, J.Y. Gan, T.S. Chin, T.T. Shun, C.H. Tsau, S.Y. Chang, Nanostructured high-entropy alloys with multiple principal elements: Novel alloy design concepts and outcomes, *Adv. Eng. Mater.* 6 (2004) 299–303, <https://doi.org/10.1002/adem.200300567>
- [11] J. Yeh, S. Chen, J. Gan, S. Lin, T. Chin, Communications: formation of simple crystal structures in Cu-Co-Ni-Cr-Al-Fe-Ti-V alloys with multiprincipal metallic elements, *Metall. Mater. Trans. A* 35 (2010) 2533–2536.
- [12] G. Hillel, L. Natovitz, S. Salhov, S. Haroush, M. Pinkas, L. Meshi, Understanding the role of the constituting elements of the alccofeni high entropy alloy through the investigation of quaternary alloys, *Metals* 10 (2020) 1–11, <https://doi.org/10.3390/met10101275>
- [13] L.J. Santodonato, P.K. Liaw, R.R. Unocic, H. Bei, J.R. Morris, Predictive multiphase evolution in Al-containing high-entropy alloys, *Nat. Commun.* 9 (2018) 1–10, <https://doi.org/10.1038/s41467-018-06757-2>
- [14] S. Huang, Á. Vida, D. Molnár, K. Kádás, L. Károly Varga, E. Holmström, L. Vitos, Phase stability and magnetic behavior of FeCrCoNiGe high-entropy alloy, *Appl. Phys. Lett.* 107 (2015) 1–5, <https://doi.org/10.1063/1.4938398>
- [15] J. Cieslak, J. Tobola, K. Berent, M. Marciszko, Phase composition of AlxFeNiCrCo high entropy alloys prepared by sintering and arc-melting methods, *J. Alloy. Compd.* 740 (2018) 264–272, <https://doi.org/10.1016/j.jallcom.2017.12.333>
- [16] H. Chou, Y. Chang, S. Chen, J. Yeh, Microstructure, thermophysical and electrical properties in AlxCoCrFeNi (0 ≤ x ≤ 2) high-entropy alloys, *Mater. Sci. Eng. B* 163 (2009) 184–189, <https://doi.org/10.1016/j.mseb.2009.05.024>
- [17] L. Meshi, Y. Linden, A. Munitz, S. Salhov, M. Pinkas, Retardation of the σ phase formation in the AlCoCrFeNi multi-component alloy, *Mater. Charact.* 148 (2019) 171–177, <https://doi.org/10.1016/j.matchar.2018.12.010>
- [18] D. Karlsson, A. Marshal, F. Johansson, M. Schuisky, M. Sahlberg, J.M. Schneider, U. Jansson, Elemental segregation in an AlCoCrFeNi high-entropy alloy – A comparison between selective laser melting and induction melting, *J. Alloy. Compd.* 784 (2019) 195–203, <https://doi.org/10.1016/j.jallcom.2018.12.267>
- [19] V. Shivam, Y. Shadangi, J. Basu, N.K. Mukhopadhyay, Evolution of phases, hardness and magnetic properties of AlCoCrFeNi high entropy alloy processed by mechanical alloying, *J. Alloy. Compd.* 832 (2020) 1–7, <https://doi.org/10.1016/j.jallcom.2020.154826>
- [20] K.C. Cheng, J.H. Chen, S. Stadler, S.H. Chen, Properties of atomized AlCoCrFeNi high-entropy alloy powders and their phase-adjustable coatings prepared via plasma spray process, *Appl. Surf. Sci.* 478 (2019) 478–486, <https://doi.org/10.1016/j.apsusc.2019.01.203>
- [21] A. Manzoni, H. Daoud, R. Völkl, U. Glatzel, N. Wanderka, Phase separation in equiatomic AlCoCrFeNi high-entropy alloy, *Ultramicroscopy* 132 (2013) 212–215, <https://doi.org/10.1016/j.ultramic.2012.12.015>
- [22] S. Gražulis, A. Daškevič, A. Merkyš, D. Chateigner, L. Lutterotti, M. Quirós, N.R. Serebryanaya, P. Moeck, R.T. Downs, A. Le Bail, Crystallography Open Database (COD): an open-access collection of crystal structures and platform for world-wide collaboration, *Nucleic Acids Res* 40 (2012) 420–427, <https://doi.org/10.1093/nar/gkr900>
- [23] S. Graulis, D. Chateigner, R.T. Downs, A.F.T. Yokochi, M. Quirós, L. Lutterotti, E. Manakova, J. Butkus, P. Moeck, A. Le Bail, Crystallography open database – an open-access collection of crystal structures, *J. Appl. Crystallogr* 42 (2009) 726–729, <https://doi.org/10.1107/S0021889809016690>
- [24] S. Lee, A. Masood, T. Tamaki, V. Strom, K.V. Rao, A. Makino, A. Inoue, Magneto-thermo-gravimetric technique to investigate the structural and magnetic properties of Fe-B-Nb-Y bulk metallic glass, *J. Phys. Conf. Ser.* 144 (2009) 1–4, <https://doi.org/10.1088/1742-6596/144/1/012074>
- [25] S.R. Larsen, D. Hedlund, H. Stopfel, D. Karlsson, C.K. Christensen, P. Svedlindh, J. Cedervall, Magnetic properties and thermal stability of B2 and bcc phases in AlCoCrFeMnNi, *J. Alloy. Compd.* 861 (2021) 158450, <https://doi.org/10.1016/j.jallcom.2020.158450>
- [26] Y. Ma, B. Jiang, C. Li, Q. Wang, C. Dong, P.K. Liaw, F. Xu, L. Sun, The BCC/B2 morphologies in AlxNiCoFeCr high-entropy alloys, *Metals* 7 (2017) 1–12, <https://doi.org/10.3390/met7020057>
- [27] H. Kaneko, M. Homma, K. Nakamura, M. Okada, G. Thomas, Phase diagram of Fe-Cr-Co permanent magnet system, *IEEE Trans. Magn.* 13 (1977) 1325–1327, <https://doi.org/10.1109/TMAG.1977.1059557>
- [28] B.O. Mukhamedov, A.V. Ponomareva, I.A. Abrikosov, Spinodal decomposition in ternary Fe-Cr-Co system, *J. Alloy. Compd.* 695 (2017) 250–256, <https://doi.org/10.1016/j.jallcom.2016.10.185>
- [29] S. Singh, N. Wanderka, K. Kiefer, K. Siemensmeyer, J. Banhart, Effect of decomposition of the Cr-Fe-Co rich phase of AlCoCrCuFeNi high entropy alloy on magnetic properties, *Ultramicroscopy* 111 (2011) 619–622, <https://doi.org/10.1016/j.ultramic.2010.12.001>
- [30] S. Huang, W. Li, X. Li, S. Schönecker, L. Bergqvist, E. Holmström, L.K. Varga, L. Vitos, Mechanism of magnetic transition in FeCrCoNi-based high entropy alloys, *Mater. Des.* 103 (2016) 71–74, <https://doi.org/10.1016/j.matdes.2016.04.053>